Sensitive detection of sodium in a flame using parametric four-wave mixing and seeded parametric four-wave mixing

Mark J. Fernée,[1] Peter F. Barker,[2,*] Alan E. W. Knight,[1] and Halina Rubinsztein-Dunlop[2]
[1]*Molecular Dynamics Laboratory, Faculty of Science and Technology, Griffith University, Nathan, Queensland 4111, Australia*
[2]*Laser Science Centre, Physics Department, University of Queensland, St. Lucia, Queensland 4072, Australia*
(Received 15 September 1997)

Two-photon resonant parametric four-wave mixing and a newly developed variant called seeded parametric four-wave mixing are used to detect trace quantities of sodium in a flame. Both techniques are simple, requiring only a single laser to generate a signal beam at a different wavelength which propagates collinearly with the pump beam, allowing efficient signal recovery. A comparison of the two techniques reveals that seeded parametric four-wave mixing is more than two orders of magnitude more sensitive than parametric four-wave mixing, with an estimated detection sensitivity of 5×10^9 atoms/cm^3. Seeded parametric four-wave mixing is achieved by cascading two parametric four-wave mixing media such that one of the parametric fields generated in the first high-density medium is then used to ''seed'' the same four-wave mixing process in a second medium in order to increase the four-wave mixing gain. The behavior of this seeded parametric four-wave mixing is described using semiclassical perturbation theory. A simplified small-signal theory is found to model most of the data satisfactorily. However, an anomalous saturationlike behavior is observed in the large signal regime. The full perturbation treatment, which includes the competition between two different four-wave mixing processes coupled via the signal field, accounts for this apparently anomalous behavior. [S1050-2947(98)03903-1]

PACS number(s): 42.65.Ky, 32.80.−t

I. INTRODUCTION

The remote sensing of atoms and molecules is important for a large number of applications where restrictions to access, environmental hazards, and other factors prevent the use of direct detection methods. Optical techniques offer some of the best possibilities for remote sensing, being largely noninvasive and nonperturbative. However, there is no single optical technique that is suited to all applications, so the development of alternative detection strategies may provide effective solutions for certain applications. Important factors for any potential remote sensing technique are simplicity of operation and sensitivity.

The use of coherent techniques for remote sensing is particularly advantageous as the detected signal travels in a coherent beam in a direction determined by the phase matching conditions in the medium. This enables efficient recovery of the signal, even over relatively long distances. Degenerate four-wave mixing (DFWM) and related coherent nonlinear techniques based on resonance enhancement of the nonlinear refractive index have found increasing application in combustion diagnostics and remote sensing applications, providing good spatial resolution and high sensitivity [1]. However, these techniques tend to provide such benefits at the expense of simplicity, normally requiring multiple beams to achieve the appropriate phase matching and often requiring multiple colors. Furthermore, these techniques generally involve significant population transfer due to strong resonance enhancement and are therefore susceptible to and limited by saturation effects. Currently there appears to be no nonlinear technique that requires only a single (undivided) pump beam and is suitable for trace species detection.

DFWM and its variants form a special class of four-wave mixing (FWM) that may be interpreted in terms of diffraction from a laser-induced grating formed within the nonlinear medium [2]. However, in general FWM is a property of the nonlinear response of the polarization of the medium and cannot necessarily be interpreted in terms of a laser-induced grating. Two-photon resonant parametric four-wave mixing (PFWM) is a member of this more general class. PFWM involves two-photon resonant pumping of the upper state in a three-level system. Both the upper state and ground state are dipole coupled to an intermediate state, through which a transition back to the ground state can occur. This produces two new fields which are nearly resonant with the intermediate state and which are generated simultaneously, both starting from zero-point fluctuations [3].

PFWM in atomic species has been studied extensively for nonlinear frequency conversion in high-density systems where the nonlinear susceptibility can be made sufficiently large [4]. PFWM also offers some unique advantages for this class of nonlinear technique, such as only requiring a single laser beam and returning a coherent signal at a frequency different from, but in most circumstances traveling collinearly with the pump laser. Such a technique would minimize the optical access requirement and simplify signal retrieval and as such be strongly suited to remote sensing if it were sufficiently sensitive. In previous applications the medium density could always be increased to a point where efficient FWM is achieved; hence until now, sensitivity has not been an issue of concern. Considering PFWM must simultaneously generate two different fields using two-photon resonant pumping, with both fields starting from zero-point

*Present address: Department of Mechanical and Aerospace Engineering, Princeton University, Princeton, NJ.

fluctuations, we would expect its sensitivity to be far below that attainable using alternative strategies. However, as PFWM involves pumping a two-photon resonant transition it can be operated with greater pump powers without significant population transfer and saturation effects occurring. Although other strong-field effects eventually limit the gain, PFWM can nevertheless be operated with pump powers orders of magnitude above the saturation threshold of resonant techniques in order to increase its sensitivity.

PFWM is readily achieved in most atomic species as there usually exist atomic states of the appropriate parity to facilitate the interaction. This can be illustrated by sodium where PFWM has been reported using two-photon excitation of the $3s \rightarrow 4s$, $3s \rightarrow 4d$, $3s \rightarrow 5s$, $3s \rightarrow 3d$ transitions [5–7]. In fact, as PFWM is commonly used for nonlinear frequency conversion to vacuum ultraviolet wavelengths, a large array of different transitions in many atomic species have been investigated for this purpose [4].

As PFWM is a FWM process where only two fields are initially supplied and the remaining two fields must be generated via the PFWM interaction, it would be reasonable to expect that if one of the two generated fields were initially provided along with the pump field, the gain of the process would increase significantly. The use of a strong seeder field to increase the gain and efficiency of nonlinear frequency conversion has already been suggested [8,9] and demonstrated experimentally [10–12] in the strong-field regime. These studies produced the seeder field using a second laser source. However, the complication of requiring two laser sources tends to compromise the usefulness of the technique for remote sensing. Fortunately a simple solution presents itself: By cascading two PFWM media, the first medium can be used to generate the extra field to be used in the next PFWM medium. This simply requires the use of a filter to remove the other unwanted PFWM field, passing both the pump and what we term the seeder field. We refer to this cascaded process based on PFWM transitions as seeded parametric four-wave mixing (SPFWM).

Our previous demonstration of SPFWM in nitric oxide [13] revealed an increase in FWM gain of over four orders of magnitude compared to PFWM alone, providing the ability to detect trace quantities of NO. The simplicity of SPFWM was displayed in the ability to measure the rotationally resolved $C^2\Pi \leftarrow X^2\Pi(0 \leftarrow 0)$ spectrum of NO by simply scanning the pump laser. SPFWM has also been used to detect nitric oxide generated in an air-acetylene flame, where the seeder field was provided by PFWM in a high-pressure nitric oxide cell, indicating the ability to phase match in harsh environments [14].

In this paper we study PFWM and SPFWM in sodium nebulized into a flame in order to characterize the techniques in combustion environments and determine the respective detection limits. An understanding of SPFWM behavior is obtained through modeling the FWM process using semiclassical perturbation theory. Due to the complexity of the sodium system studied, a five-level model is required which includes contributions from a secondary or parasitic FWM process. It is the complex dynamical behavior of the five-level model which best describes the observed behavior of the SPFWM signal.

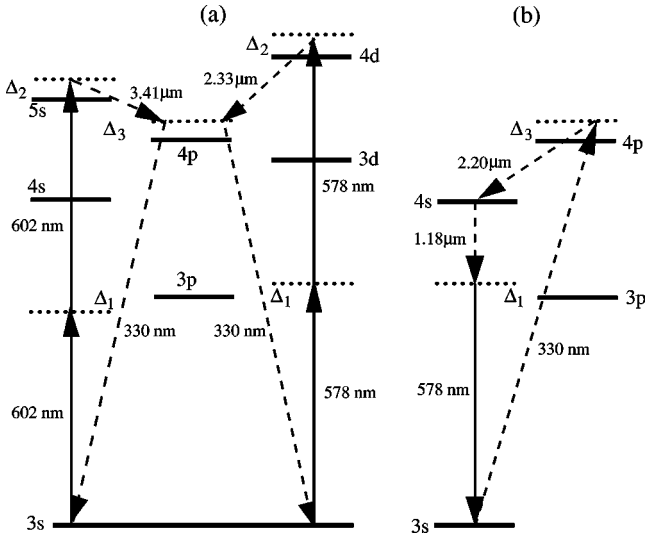

FIG. 1. (a) The sodium level scheme used for PFWM via two-photon pumping of the $3s \rightarrow 5s$ and $3s \rightarrow 4d$ transitions. The relevant detunings are also indicated. Δ_1 is the average detuning of the pump from the intermediate $3p$ states, representing the strongest term in the sum over intermediate states contained in the two-photon coupling term. Δ_2 is the detuning of the pump from the two-photon resonance and Δ_3 the detuning of the signal fields from the intermediate $4p$ state which results from phase matching requirements. (Note: The infrared wavelengths indicated correspond to a detuning, $\Delta_2 = 0$.) (b) The sodium levels responsible for a secondary parasitic FWM process. All the dashed lines represent photons that must be generated by the medium. This FWM process occurs due to the stimulated Raman scattering of the 330 nm field producing the 2.20 μm field, which acts to produce the 1.18 μm field through FWM with the pump field. The 1.18 μm field does not phase match collinearly and so travels in a cone around the pump beam.

II. A PFWM MODEL FOR SODIUM

The process of resonance enhanced PFWM generally requires at least a three-level ladder quantum system with the middle-level dipole coupled to both the upper and lower levels (although PFWM has been observed in a strongly driven two-level system via the induced Rabi sidebands [15,16]). When such a system is driven by a strong laser field which is two-photon resonant with the ground and upper states, it can give rise to FWM by the simultaneous emission of two photons which satisfy phase matching requirements and are nearly resonant with the two intermediate transitions. If the intermediate level is positioned asymmetrically in energy with respect to the upper and lower levels, the emitted photons will be emitted at wavelengths which are both longer and shorter than that of the pump photons. Two of these transitions observed in sodium are depicted in Fig. 1(a) corresponding to two-photon pumping of the $3s \rightarrow 5s$ and $3s \rightarrow 4d$ transitions.

SPFWM involves the cascading of two FWM media. The first FWM medium, termed the seeder, is a high-density medium which is used to generate a strong infrared field (via PFWM) which is used to seed the PFWM process in the next stage of the experiment. The infrared seeder field travels collinearly with the pump field into the low-density medium where the signal field is generated. As the signal is generated

via the same PFWM transition as that used for the generation of the seeder field, the signal behavior may be modeled using the same coupled field equations as those used to describe the PFWM, with an appropriate modification of the initial conditions.

In Fig. 1(b) we indicate an extra (parasitic) FWM process that can occur due to stimulated Raman scattering of the 330-nm PFWM signal to the sodium $4s$ level. The 578-nm pump field, 330-nm PFWM signal field, and the Raman field then undergo FWM to generate a signal at 1.18 μm. Emission at 2.20 μm has been detected and attributed to the stimulated Raman field and anomalous emission at 1.18 μm has been detected and attributed to the secondary FWM process that occurs due to the presence of the other three fields [5,7]. These extra fields are important in our case because, if they are generated in the PFWM section of our experiment, they will propagate with the pump beam in a similar fashion to the infrared PFWM signal. These other infrared fields must be considered as extra input fields when modeling the SPFWM process.

A. Nonlinear field evolution equations

The nonlinear evolution of the electric fields can be described using Maxwell's equations in the slowly varying envelope approximation. For plane-wave propagation these are given by

$$\frac{\partial \mathcal{E}_k(z)}{\partial z} = \frac{i\, n(\omega_k)\omega_k}{2\varepsilon c}\mathcal{P}_k^{\mathrm{NL}}(z), \tag{1}$$

where $\mathcal{E}_k(z)$ is a plane-wave Fourier component of the electric field at a frequency ω_k propagating in the z direction, $\mathcal{P}_k^{\mathrm{NL}}(z)$ is the associated Fourier component of the nonlinear polarization, $n(\omega_k)$ is the refractive index of the medium, and all other symbols have their usual meaning.

The nonlinear polarization is usually expressed in terms of a nonlinear susceptibility $\chi^{(3)}$ as follows:

$$P^{\mathrm{NL}} = \varepsilon_0 \chi^{(3)} E^3. \tag{2}$$

When the electric field is written as a Fourier series, the different nonlinear processes can be readily identified using this notation.

To proceed further, the nonlinear medium itself must be considered. The medium polarization can be calculated from the density matrix describing the medium by calculating the trace of the density matrix $\rho(t)$ with the electric dipole operator μ,

$$P(t) = N\overline{\mathrm{Tr}[\rho(t)\mu]}, \tag{3}$$

where N is the number of atoms in the interaction region and the bar over the trace represents an orientation average corresponding to an ensemble of atoms with random orientations with respect to the field. For nonlinear interactions, this average is not always easy to calculate; however, in our case it simply represents a scaling factor which can be neglected.

The calculation of the appropriate density matrix elements is accomplished by solving the density-matrix equations of motion

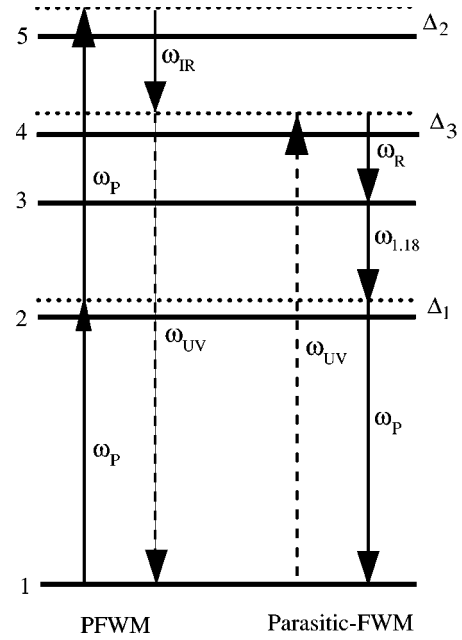

FIG. 2. The levels and detunings used for modeling the SPFWM in sodium. We model the $3s \rightarrow 4d$ pumping scheme in accordance with our experiment, so level 5 corresponds to the $4d$ level. Photons represented by solid lines represent fields that are present initially and the ω_{UV} field is generated by FWM in the medium. In this case the ω_{IR} and ω_R fields are supplied at wavelengths near 2.33 and 2.20 μm, respectively, and the $\omega_{1.18}$ field corresponds to a wavelength of 1.18 μm. The fine splitting of the $4p$ state is not shown here as each fine splitting component essentially behaves independently of the other and so is modeled separately.

$$i\hbar \frac{\partial \rho(t)}{\partial t} = [H, \rho(t)], \tag{4}$$

where H is the total system Hamiltonian which, in the limit of weak interaction, can be expressed in terms of a free Hamiltonian representing the unperturbed energy levels of the system and an interaction Hamiltonian. In the electric dipole approximation, the interaction Hamiltonian H_I represents the interaction of the electric dipole with the electric field, via

$$H_I = -\mu E. \tag{5}$$

By solving the density-matrix equation of motion, Eq. (4), the medium polarization and hence the equations for the evolution of the field can be determined. In general, the solution of Eq. (4) is extremely complicated. However, for weak interactions, the density-matrix equation may be solved perturbatively [17]. Solutions to third order are necessary to describe FWM.

We consider the five-level sodium system depicted in Fig. 2 which includes both PFWM and parasitic-FWM processes. Using the third-order perturbation solutions for the density-matrix evolution and retaining only near-resonant terms, the appropriate polarization components have been derived and substituted into the slowly varying envelope equation (1) to obtain the field evolution equations. As this approach was extensively developed elsewhere [18], we only give the re-

sults here. In the case where we can neglect pump field depletion, the coupled amplitude and phase equations are given by

$$\frac{dA_{\mathrm{IR}}}{dz}=\frac{\omega_{\mathrm{IR}}}{2\varepsilon_0 c}(-|\chi_{\mathrm{FWM1}}|A_P^2A_{\mathrm{UV}}\cos\Theta_1-\mathrm{Im}\chi_{\mathrm{TPA1}}A_{\mathrm{UV}}^2A_{\mathrm{IR}}), \tag{6a}$$

$$\frac{dA_{\mathrm{UV}}}{dz}=\frac{\omega_{\mathrm{UV}}}{2\varepsilon_0 c}(-|\chi_{\mathrm{FWM1}}|A_{\mathrm{IR}}A_P^2\cos\Theta_1-|\chi_{\mathrm{FWM2}}|A_{1.18}A_RA_P \times\cos\Theta_2-\mathrm{Im}\chi_{\mathrm{TPA1}}A_{\mathrm{UV}}A_{\mathrm{IR}}^2-\mathrm{Im}\chi_{\mathrm{SRS}}A_{\mathrm{UV}}A_R^2), \tag{6b}$$

$$\frac{dA_{1.18}}{dz}=\frac{\omega_{1.18}}{2\varepsilon_0 c}(-|\chi_{\mathrm{FWM2}}|A_PA_{\mathrm{UV}}A_R\cos\Theta_2 -\mathrm{Im}\chi_{\mathrm{TPA2}}A_P^2A_{1.18}), \tag{6c}$$

$$\frac{dA_R}{dz}=\frac{\omega_R}{2\varepsilon_0 c}(|\chi_{\mathrm{FWM2}}|A_PA_{1.18}A_{\mathrm{UV}}\cos\Theta_2+\mathrm{Im}\chi_{\mathrm{SRS}}A_{\mathrm{UV}}^2A_R), \tag{6d}$$

$$\frac{d\Theta_1}{dz}=\frac{1}{2\varepsilon_0 c}|\chi_{\mathrm{FWM1}}|\sin\Theta_1A_P^2\left(\frac{\omega_{\mathrm{IR}}A_{\mathrm{UV}}}{A_{\mathrm{IR}}}+\frac{\omega_{\mathrm{UV}}A_{\mathrm{IR}}}{A_{\mathrm{UV}}}\right) +\frac{1}{2\varepsilon_0 c}|\chi_{\mathrm{FWM2}}|\sin\Theta_2A_P\frac{\omega_{\mathrm{UV}}A_{1.18}A_R}{A_{\mathrm{UV}}}, \tag{6e}$$

$$\frac{d\Theta_2}{dz}=\frac{1}{2\varepsilon_0 c}|\chi_{\mathrm{FWM1}}|\sin\Theta_1A_P^2\frac{\omega_{\mathrm{UV}}A_{\mathrm{IR}}}{A_{\mathrm{UV}}} +\frac{1}{2\varepsilon_0 c}|\chi_{\mathrm{FWM2}}|\sin\Theta_2A_P\left(\frac{\omega_{\mathrm{UV}}A_{1.18}A_R}{A_{\mathrm{UV}}} +\frac{\omega_{1.18}A_{\mathrm{UV}}A_R}{A_{1.18}}-\frac{\omega_RA_{\mathrm{UV}}A_{1.18}}{A_R}\right), \tag{6f}$$

where the A_x's represent the real field amplitudes defined by $\vec{\mathcal{E}}_x=A_x\,e^{i\phi_x}$, where $\mathcal{E}_x$ is the complex field amplitude and ϕ_x is the associated phase of the field. A_P represents the pump field amplitude which is a constant. A_{UV} and A_{IR} correspond to the ultraviolet and infrared PFWM field amplitudes. A_R is the stimulated Raman field amplitude and $A_{1.18}$ is the amplitude of the associated 1.18-μm infrared field of the parasitic FWM process. The corresponding field phases are grouped into two phase terms (with the pump field providing the phase reference); $\Theta_1=\phi_{\mathrm{UV}}+\phi_{\mathrm{IR}}+\phi_{\chi_{\mathrm{FWM1}}}$ and $\Theta_2=\phi_{\mathrm{UV}}-\phi_R-\phi_{1.18}-\phi_{\chi_{\mathrm{FWM2}}}$. The field phases are easily recognized and of the remaining two phases, $\phi_{\chi_{\mathrm{FWM1}}}$ corresponds to the phase of the complex PFWM susceptibility and $\phi_{\chi_{\mathrm{FWM2}}}$ corresponds to the phase of the complex parasitic FWM susceptibility. If required, these phases could include a phase matching term of the form $\Delta k_{\mathrm{FWM}}\,z$ which under poor phase matching conditions contributes a highly oscillatory factor, which can integrate to zero over long interaction lengths. For this paper we primarily consider perfect phase matching $\Delta k_{\mathrm{FWM}}=0$.

The various susceptibilities in Eq. (6) represent the different near-resonant nonlinear processes obtained in a third-order perturbation treatment of the system with χ_{FWM1} and χ_{FWM2} representing the PFWM and parasitic four-wave mixing processes, respectively, χ_{TPA1} represents two-photon absorption of the generated PFWM fields, and χ_{TPA2} represents two-photon absorption of the pump and 1.18-μm fields in the parasitic FWM process, and χ_{SRS} represents stimulated Raman scattering of the PFWM signal field to produce the Raman field. These susceptibilities are directly proportional to the sodium number density and depend on the various dipole matrix elements and field detunings as follows:

$$\chi_{\mathrm{FWM1}}=N\left[\frac{\mu_{12}\mu_{25}\mu_{54}\mu_{41}}{\hbar^3\Delta_1\Delta_3(\Delta_2-i\Gamma_{51})}\right], \tag{7a}$$

$$\chi_{\mathrm{FWM2}}=iN\left[\frac{\mu_{14}\mu_{43}\mu_{32}\mu_{21}}{\hbar^3\Delta_1\Delta_3\Gamma_{31}}\right], \tag{7b}$$

$$\chi_{\mathrm{TPA1}}=N\left[\frac{|\mu_{14}|^2|\mu_{45}|^2}{\hbar^3\Delta_3^2(\Delta_2-i\Gamma_{51})}\right], \tag{7c}$$

$$\chi_{\mathrm{TPA2}}=iN\left[\frac{|\mu_{12}|^2|\mu_{23}|^2}{\hbar^3\Delta_1^2\Gamma_{31}}\right], \tag{7d}$$

$$\chi_{\mathrm{SRS}}=iN\left[\frac{|\mu_{14}|^2|\mu_{43}|^2}{\hbar^3\Delta_3^2\Gamma_{31}}\right], \tag{7e}$$

where N is the sodium number density, the μ_{ij}'s are the dipole matrix elements connecting the levels $|i\rangle$ and $|j\rangle$ according to the five-level model of Fig. 2, and Γ_{ij}'s represent the various transition linewidths (half-width) which are included phenomenologically in this semiclassical treatment.

We note that the Eqs. (6) do not contain any linear absorption terms. This approximation assumes that the relevant fields are generated sufficiently far from resonance such that we can ignore direct absorption. We have also set the various refractive indices to unity in the propagation equations (6), which is a reasonable approximation in a low-density gaseous medium. Other terms that should be present in the coupled amplitude equations, such as ac Stark shift, multiphoton ionization, and other higher-order nonlinear terms have also been ignored. These terms represent strong-field effects and we assume that they have no significant effect on the FWM field evolution.

Laser bandwidth and Doppler broadening effects are also omitted in Eqs. (6), as we are only considering the case of exact two-photon resonant pumping where these effects simply contribute a constant factor. Doppler broadening and the laser bandwidth only need to be considered if the spectral behavior of signal is to be modeled.

B. Unperturbed PFWM and SPFWM behavior

Although Eqs. (6) represent the interaction of two FWM processes, if we neglect the 1.18 μm and Raman fields leaving the ultraviolet and infrared PFWM fields and the associated Θ_1 phase, we can then readily simplify the equations in order to understand the behavior of the unperturbed PFWM

and SPFWM processes. Under these conditions, the phase Θ_1 rapidly approaches a steady state over a distance far shorter than the characteristic interaction length of the field amplitudes, in which case $\Theta_1=\pi$ can be substituted into the amplitude equations resulting in the FWM term and the two-photon absorption term acting out of phase. Equations (6) then reduce to

$$\frac{dA_{\mathrm{IR}}}{dz}=\frac{\omega_{\mathrm{IR}}}{2\varepsilon_0 c}(|\chi_{\mathrm{FWM1}}|A_P^2A_{\mathrm{UV}}-\mathrm{Im}\chi_{\mathrm{TPA1}}A_{\mathrm{UV}}^2A_{\mathrm{IR}}), \quad (8a)$$

$$\frac{dA_{\mathrm{UV}}}{dz}=\frac{\omega_{\mathrm{UV}}}{2\varepsilon_0 c}(|\chi_{\mathrm{FWM1}}|A_{\mathrm{IR}}A_P^2-\mathrm{Im}\chi_{\mathrm{TPA1}}A_{\mathrm{UV}}A_{\mathrm{IR}}^2). \quad (8b)$$

The simplified field evolution equations (8) can be decoupled and solved using the following constant of the motion:

$$\frac{A_{\mathrm{IR}}^2}{\omega_{\mathrm{IR}}}-\frac{A_{\mathrm{UV}}^2}{\omega_{\mathrm{UV}}}=\mathrm{const.} \quad (9)$$

The constant of the motion results from production of photons in pairs and corresponds to the difference in photon number between the two fields being a constant. We wish to consider the case corresponding to PFWM, where both the UV and IR fields evolve from zero-point fluctuations and the case corresponding to SPFWM, where a strong IR seeder field is present initially.

C. Small signal solutions

For the case of PFWM, where both fields start from zero-point fluctuations, the constant of the motion must be zero, whereas when a strong seeder field is initially present and only the signal field must start from the zero-point fluctuations, the constant is simply given by $n(\omega_{\mathrm{IR}})A_{\mathrm{IR}}^2(0)/\omega_{\mathrm{IR}}$, where $A_{\mathrm{IR}}(0)$ is the initial amplitude of the seeder field.

For PFWM we find the small signal behavior is approximated by

$$A_{\mathrm{UV}}(z)\approx A_{\mathrm{UV}}(0)\exp[(1/2\varepsilon_0 c)\ \sqrt{\omega_{\mathrm{UV}}\omega_{\mathrm{IR}}}\ |\chi_{\mathrm{FWM1}}|\ A_P^2\ z]. \quad (10)$$

While this solution exhibits exponential gain in the small signal regime, it is nonetheless governed by the initial amplitude of the signal field which is vanishingly small. Therefore an appreciable gain length is required for the signal field to grow to a significant value. This gain length is inversely proportional to both the pump intensity and the density of the medium, such that by using a high-density medium and high pump intensities a reasonable gain length can be achieved. However, high number densities are contrary to our requirement and high pump intensities can cause other problems such as population transfer which destroys the phase matching.

In order to significantly increase the gain of the process for use with low number densities we supply a strong initial IR field. For this SPFWM the small signal behavior is readily approximated as

$$A_{\mathrm{UV}}(z)\approx\frac{\omega_{UV}}{2\varepsilon_0 c}|\chi_{\mathrm{FWM1}}|A_{\mathrm{IR}}(0)A_P^2 z. \quad (11)$$

Here we find that the behavior of the seeded system is independent of the amplitude of the initial signal field $A_{\mathrm{UV}}(0)$. We immediately see that the signal intensity will be proportional to the square of the number density N rather than the exponential dependence of PFWM. The signal intensity will also be proportional to the square of the pump intensity and directly proportional to the seeder intensity.

D. Seeder operation in the two-photon cancellation regime

The gain of the high-density seeder medium can be made sufficiently large such that the PFWM operates in what is termed the two-photon cancellation regime. This is characterized by the condition where two-photon absorption of the pump field occurs out of phase with and balances the two-photon absorption of the generated parametric fields, such that population transfer to the excited state is suppressed [18,7]. The two-photon cancellation regime is defined by the following condition:

$$A_P^2-\frac{\mathrm{Im}\chi_{\mathrm{TPA1}}}{|\chi_{\mathrm{FWM1}}|}A_{\mathrm{UV}}A_{\mathrm{IR}}=0. \quad (12)$$

When this condition is satisfied and using the fact that the UV and IR fields must be proportional to each other due to the paired photon generation, both the parametric signal fields become linearly proportional to the pump field. Operation in the two-photon cancellation regime is a condition that may be achieved in the seeder PFWM stage where high atomic densities are used. Operation in this regime has been demonstrated in the high atomic densities obtainable using a sodium heat pipe [7]. If the seeder is operated in this two-photon cancellation regime and absorption of the UV signal is negligible, we can expect the small signal behavior of the SPFWM signal intensity to be proportional to the cube of the pump intensity.

When the parasitic FWM process is included, the two-photon cancellation regime is no longer valid. However, numerical simulations of the field evolution indicate that for conditions found in the high gain seeder medium, the coupled FWM processes will evolve to steady state such that all the field amplitudes scale in direct proportion to the pump field amplitude. Under these conditions the signal interpretation remains the same.

E. Phase mismatching tolerances for PFWM and SPFWM

It was mentioned that a phase matching term can be included in the phase of the FWM susceptibility. We have chosen the case of perfect phase matching to illustrate the behavior of the system as this represents the case of greatest gain for the PFWM process. However, some sense of how critical are the phase matching requirements can be obtained from inspection of the coupled equations (6). An indication of how large the phase mismatch can be without significant reduction in the output signal is given by an abstract quantity which we refer to as the characteristic length of the process z_c. The larger the characteristic length, the smaller the phase mismatch that can be tolerated. Such characteristic lengths can be ascertained from the small signal solutions to the coupled equations (8). The associated phase mismatch toler-

ance is proportional to the inverse of the characteristic length. For the PFWM process, from Eq. (10) we find

$$z_c \approx \left(\frac{\omega_{\mathrm{UV}}}{2\varepsilon_0 c} |\chi_{\mathrm{FWM1}}|\, A_P^2 \right)^{-1} \tag{13}$$

and for the SPFWM process, from Eq. (11) we find

$$z_c \approx \left(\frac{\omega_{\mathrm{UV}}}{2\varepsilon_0 c} |\chi_{\mathrm{FWM1}}| A_{\mathrm{IR}}(0) A_P^2 \right)^{-1}. \tag{14}$$

It is immediately apparent that the SPFWM process will tolerate a greater phase mismatch in comparison to the PFWM process due to the extra seeder field amplitude factor A_{IR}. However, for PFWM in the high-density seeder medium, $|\chi_{\mathrm{FWM1}}|$ can be many orders of magnitude greater than the susceptibility in the low-density SPFWM media. In this case the larger phase mismatch allowance induced by the seeder field can compensate for the reduced characteristic length due to the low atomic density. This suggests that phase matching requirements in the SPFWM section are not so stringent, such that both the high-density seeder process and the low-density SPFWM process should at least share similar phase mismatching tolerances. Furthermore, we see that the tolerance of SPFWM to phase mismatches increases with increasing seeder field strength. This is an important property when operating in environments where the presence of other species affects phase matching.

F. SPFWM field evolution: Numerical modelling

Numerical modeling of the SPFWM process using the five-level system, including the two interacting FWM processes described by Eqs. (6), is readily accomplished using standard numerical integration routines. This requires specifying the initial field amplitudes and phases. The initial field amplitudes are directly input as user specified parameters. However, the starting phases are not so easily specified. The phase equations (6e) and (6f) evolve significantly over a much shorter distance than the amplitude equations, such that an arbitrary specification of the phases would require an integration step size orders of magnitude smaller than that required for the amplitude equations. Due to the coupling of the two FWM processes, the phases do not rapidly evolve to a steady state. However, this is approximately the case over short times when the A_{UV} field is much smaller than the other fields. In this case the phases rapidly reach a quasi-steady state which is defined by

$$\sin\Theta_1 = -\frac{|\chi_{\mathrm{FWM2}}| A_{1.18} A_R}{|\chi_{\mathrm{FWM1}}| A_P A_{\mathrm{IR}}} \sin\Theta_2, \tag{15}$$

For SPFWM, all the initial phases apart from that corresponding to the A_{UV} field can be specified arbitrarily and as such can be randomly assigned without loss of generality. The A_{UV} field will then evolve such that the steady state (15) is satisfied. Therefore we write the steady state in terms of the UV field phase explicitly,

$$\sin(\phi_{\mathrm{UV}} + \phi_1) = -\frac{|\chi_{\mathrm{FWM2}}| A_{1.18} A_R}{|\chi_{\mathrm{FWM1}}| A_P A_{\mathrm{IR}}} \sin(\phi_{\mathrm{UV}} - \phi_2), \tag{16}$$

where the phases ϕ_1 and ϕ_2 are random constant initial phases corresponding to the phases of the initial fields and FWM susceptibilities. Equation (16) can be readily solved for ϕ_{UV} to give

$$\tan\phi_{\mathrm{UV}} = \frac{|\chi_{\mathrm{FWM2}}| A_{1.18} A_R \sin\phi_2 - |\chi_{\mathrm{FWM1}}| A_P A_{\mathrm{IR}} \sin\phi_1}{|\chi_{\mathrm{FWM2}}| A_{1.18} A_R \cos\phi_2 + |\chi_{\mathrm{FWM1}}| A_P A_{\mathrm{IR}} \cos\phi_1}. \tag{17}$$

From Eq. (17) the initial phases can be determined such that the phase evolution occurs over a similar characteristic length as the amplitude equations.

Equations (6) can represent the coupling of the two FWM processes depicted in Fig. 2. However, due to the fine structure of the $4p$ state, there are two possible FWM paths for each process (when considering coupling to the $4d$ level, other paths exist but they have nonlinear susceptibilities at least an order of magnitude weaker than the dominant paths). These two paths are approximately independent of each other (apart from coupling due to the 1.18-μm field which we ignore here, as the presence of the 1.18-μm field has a minor effect on the resultant field evolution) and so we treat them separately. The solutions are calculated after scaling Eqs. (6) with the factor

$$\left(\frac{1}{2\varepsilon_0 c} |\chi_{\mathrm{FWM1}}|\, A_P^2 \right)^{-1}, \tag{18}$$

which defines the characteristic length z_c of the coupled equations. The field amplitudes are also normalized with respect to the pump amplitude A_P.

We consider the case of pumping the $3s \rightarrow 4d$ transition on resonance so that the detuning Δ_2 vanishes. Under these conditions, the normalized initial field amplitudes, the initial phases, and the ratio of the detunings Δ_1/Δ_3 need to be determined. The other coefficients are readily obtained from sodium oscillator strengths found in the literature [19].

The field and phase evolutions are shown in Fig. 3 for the case of FWM via the $4p_{3/2}$ fine-structure component. These solutions correspond to the $4p_{3/2}$ FWM component used in the fit to the SPFWM power dependence data (shown below in Fig. 9) and correspond to a detuning ratio of 850. The solutions show evolution over 10 characteristic lengths z_c. The UV field's rapid initial growth clearly indicates the effect of the seeder field in increasing the gain of the UV signal field. Early evolution of the UV signal field over approximately the first third of a characteristic length z_c is dominated by the SPFWM interaction after which the second parasitic FWM process strongly modifies the evolution. The phase evolutions have not reached a steady state which indicates that the UV signal field has not yet reached a steady state. Again the region of approximately unperturbed UV signal field evolution is indicated in the initial behavior of the phase Θ_1.

The nature of the numerical solutions is that they are most sensitive to the detuning ratio. For the 578-nm pumping of the $3s \rightarrow 4d$ transition, the detuning ratio of 850 corresponds to phase matching at a point approximately 0.4 cm^{-1} from the $3s \rightarrow 4p_{3/2}$ resonance on the negative dispersion side, which corresponds well to what has been observed elsewhere [7].

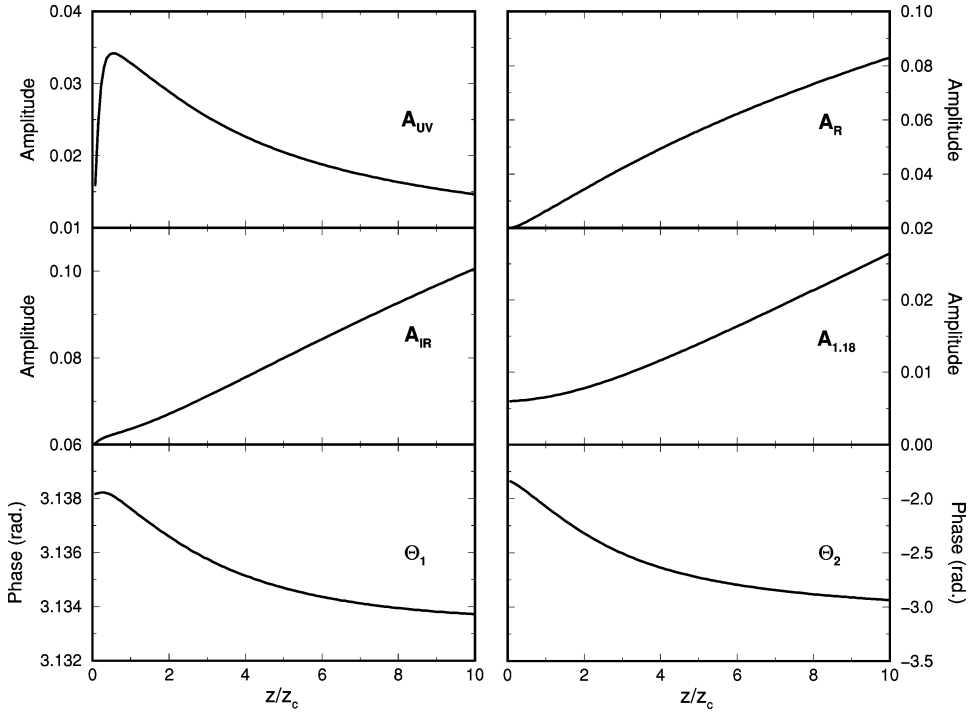

FIG. 3. The solutions of equations (6) are presented. These represent the field and phase evolutions of the FWM process that occur via the $4p_{3/2}$ state. The complete behavior of the system requires simulating FWM via both the $4p_{3/2}$ and $4p_{1/2}$ fine-structure components, calculating the respective intensity evolutions and then adding them. This solution corresponds to two-photon resonant pumping with a detuning ratio Δ_1/Δ_3 of 850. The initial field amplitudes can be determined from the graphs. The x axis is scaled by the characteristic length defined in Eq. (13).

III. THE EXPERIMENTS

The experiments involve the detection of sodium nebulized into an air-acetylene flame using PFWM and SPFWM. Slot burners (Varian AA6) were used with air-acetylene heads with a 10-cm slot length. Sodium nitrate solution, representing a known sodium concentration (ppm), was nebulized into the flame at a rate of 9.5 ± 0.5 ml/h. In order to estimate the sodium density within the flame, the flame length and width as well as the flame velocity must be known. The length of 10 cm was used as well as an estimated width of 0.6 ± 0.1 cm. The flame velocity has been measured to be 6 ± 0.5 ms^{-1}, using a sodium flow tagging technique [20] . Sodium solutions were prepared to the required concentrations with the appropriate dilution of a standard solution such that the concentration could be specified to within 10%. With these measurements and known sodium concentrations, the flame concentration of sodium can be determined to within 50%.

The 532-nm output from a neodymium-doped yttrium aluminum garnet (Nd:YAG) (Continuum NY81) laser used to pump a transversely pumped dye laser (Lambda Physik Scanmate II). Rhodamine 110 was used to generate light at around 602 nm to pump the $3s\rightarrow5s$ transition in sodium and Rhodamine 6G was used to generate light at around 578 nm to pump the $3s\rightarrow4d$ transition in sodium. For both experiments the Q switch of the Nd:YAG pump was adjusted to limit the output from the dye laser such that the operational pulse energy was limited to about 7 mJ with a pulse length of 10 nsec. This output could be attenuated with a Newport high-power variable attenuator and the beam energy monitored with a power meter (Ophir) which could be accurately placed into the beam path. The pump beam was then used in the experiment without any further modification. Thus the beam profile comprised contributions from many transverse laser modes. Spatial filtering of the pump beam, as usually employed in DFWM and other techniques requiring good spatial coherence, was not deemed necessary due to the ease of which the PFWM signal could be found. In fact spatial filtering is problematic when using these relatively high laser pulse energies.

In Fig. 4 we show the apparatus used for conducting the PFWM and SPFWM experiments. The laser beam passed through the flames approximately 15 mm above the burner heads. For the PFWM experiment, the second flame was not used and the laser was operated near 602 nm for two-photon pumping of the $3s\rightarrow5s$ transition. Laser-induced fluorescence (LIF) from the $3p$ state was simultaneously monitored at right angles to the laser beam propagation direction. The PFWM signal generated at around 330 nm was detected directly by filtering out the pump beam using UG5 Schott glass filters and a prism to separate the beams so that any residual 602 nm component could be dumped. The 330-nm signal was detected using a photomultiplier tube (EMI 9558B), the output of which was sent to a boxcar integrator (SRS), digitized with an analog-to-digital converter and stored on a computer. The 330-nm signal could be attenuated if required using a stack of glass microscope slides. 589-nm fluorescence from the $3p$ state was detected simultaneously using a 0.1-m spectrometer (Jobin Yvon H10) which was placed on its side to maximize the interaction region monitored within the flame. The 589-nm signal was detected with a photomultiplier (Hamamatsu R2007), the output of which was integrated then digitized and stored along with the PFWM data

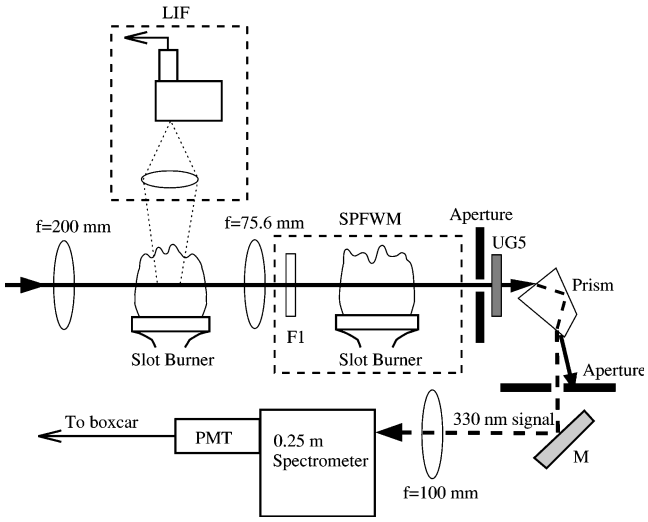

FIG. 4. The PFWM and SPFWM experimental arrangement is shown. For the PFWM experiments, LIF is also collected with a spectrometer mounted on its side to increase the detection volume and the second flame and filter are not used. The SPFWM arrangement includes a second flame and the long pass filter F1. The first flame nebulized with a high concentration sodium solution for efficient PFWM and the second with different low concentration sodium solutions. For SPFWM the recollimating lens is used to vary the focal conditions in the second flame.

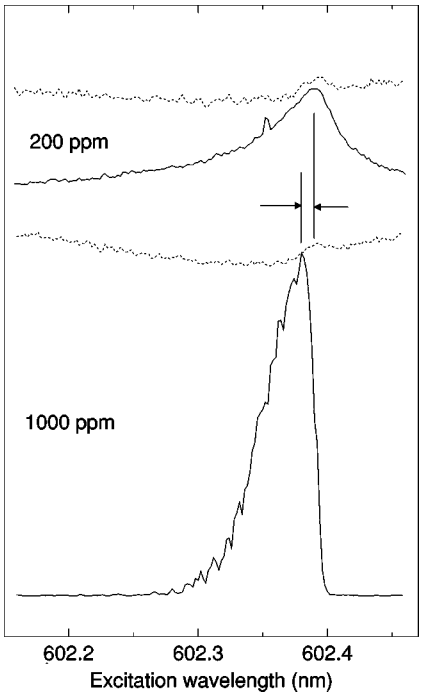

FIG. 5. The PFWM (solid lines) and LIF (dotted lines) signals observed when pumping the $3s \rightarrow 5s$ transition of sodium. Contributions from flames nebulized with a 200- and a 1000-ppm solution are displayed. The vertical axis maintains a constant scale, but the various signals are offset for clarity. The 1000-ppm PFWM signal has been strongly attenuated with 14 glass microscope slides. A shift in the PFWM resonance is also indicated for the 1000-ppm data.

on a computer. Background measurements were made from a flame nebulized with distilled water to ensure that both the PFWM and LIF signals were representative of the particular flame environment and not artifacts of a contaminated burner head.

SPFWM experiments were conducted using a slight modification to the PFWM experimental configuration. In this case two nebulized air-acetylene flames were used as shown in Fig. 4. The two lenses were used as a variable telescope to vary the focal conditions in the second flame, which was nebulized with the low concentration sodium solutions. A long pass filter (Oriel 5129), F1, was used to absorb the 330-nm PFWM signal from the first ''seeder'' flame, while transmitting both the 578-nm pump and the 2.33-μm infrared seeder field. Following the interaction in the second flame, the SPFWM generated 330-nm signal was passed by a UG5 filter while the pump and seeder fields were absorbed. Any residual field was separated by a prism and dumped. The SPFWM signal is then passed into a 0.25-m spectrometer (GCA/McPherson) and detected by a photomultiplier, with the output integrated, digitized and stored on a computer.

The SPFWM signal integrity was ensured by performing a background scan without the second flame, with the second flame but no nebulization, and finally nebulization with distilled water. The zero signal background was only obtained without any flame, with the other two conditions producing successively greater signals above the noise floor. This is primarily attributable to sodium contamination of the burner. This contamination was only a minor contribution to the signals which were obtained with the different solutions, such that small signal behavior was still observed (with a negligible contribution from contamination).

The focal conditions for the PFWM experiments corresponded to a maximum pump intensity in the interaction region of approximately 1×10^{9} W/cm^{2}. However, such high intensities are not necessary for SPFWM and so we operated with a maximum intensity no greater than 1×10^{7} W/cm^{2} in the second flame by appropriately positioning the recollimating lens. The use of a short focal length recollimating lens also acted to reduce the beam area and increase the effective gain length for SPFWM in the second flame.

IV. RESULTS AND DISCUSSION

A. Parametric four-wave mixing

The PFWM studies were conducted using the $3s \rightarrow 5s$ two-photon transition, for which a pump wavelength of approximately 602 nm was used. This corresponds to a pump photon energy below that required for single-photon or Raman excitation of any excited state of sodium. Therefore any excited-state population must result from at least two- or three-photon excitation processes such as hyper-Raman excitation. LIF was monitored from the $3p \rightarrow 3s$ transitions, expecting that $3p$ populations would result from either hyper-Raman excitation or relaxation from a higher-lying state. In any case, with two-photon resonant excitation of the $5s$ state we would expect significant spontaneous emission to the $3p$ state. Emission from both the $3p$ and $4p$ intermediate states was monitored but an appreciable LIF signal was only found around 589 nm, suggesting that very little population transfer is occurring.

In Fig. 5 we show an example of the PFWM signal along

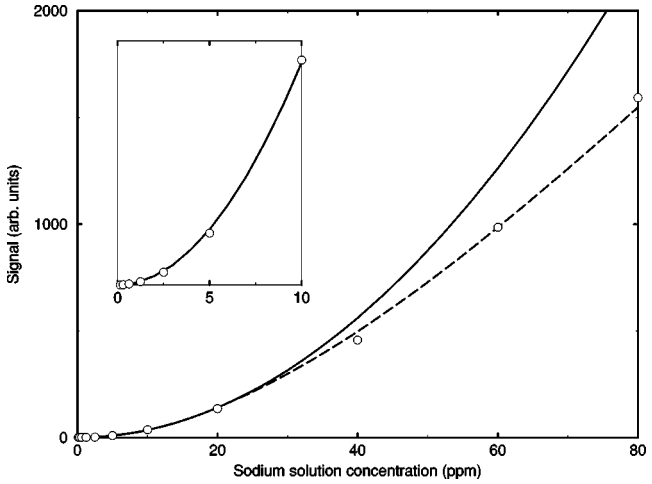

FIG. 6. The SPFWM 330 nm signal dependence on the sodium concentration in the low-density flame. The laser was fixed at 578.88 nm for resonant pumping of the $3s \rightarrow 4d$ transition with approximately 7 mJ pulses, while the seeder PFWM flame was nebulized with a 100 000 ppm solution. The experimental data are indicated by the open circles. A curve following square law scaling is fit to the data and displayed as a solid line, while the dashed line was generated using the five level model of Eqs. (6). The inset shows the small signal behavior of the data along with the square law fit curve.

with the associated LIF signal as the laser is scanned across the $3s \rightarrow 5s$ two-photon resonance. The PFWM signal shows considerable broadening and displays an asymmetry which is caused by the influence of the variation in refractive index at the pump frequency on the phase matching. The influence of the refractive index variation on the line-shape asymmetry can be seen when comparing the PFWM scan in Fig. 5 with that in Fig. 7. These two scans represent pumping of the $3s \rightarrow 5s$ and $3s \rightarrow 4d$ transitions, respectively, and they display opposite asymmetries. This is consistent with a pump frequency lying on opposite sides of the $3s \rightarrow 3p$ resonance so that the variation of refractive index affects that scan in the opposite way. This effect is not consistent with other causes such as ac Stark broadening.

The LIF scans in Fig. 5 contain both resonant and nonresonant contributions. The nonresonant LIF signal is most likely attributable to two-photon hyper-Raman scattering to the $4p$ and $3p$ states, with the $4p$ state contributing to the $3p$ emission via collisional deexcitation or cascade emission. This nonresonant emission is reduced as the pump beam approaches the two-photon resonance and the reduction is strongly correlated to the increase in PFWM signal (hence displaying a similar asymmetry). This suggests that the PFWM fields are suppressing excited-state population transfer over a broad pump laser detuning range and is most likely attributable to the suppression of stimulated electronic hyper-Raman scattering (SEHRS) in the forward direction by the PFWM fields [21]. A slight LIF peak appears when the pump laser passes through the two-photon resonance. The resonant contribution is not even as strong as the nonresonant contribution and this result barely varied with changing Na concentration in the flame as shown in Fig. 5, suggesting that two-photon resonant population of the $5s$ state is not a dominant effect. This must be the case for the efficient operation of PFWM as population transfer to higher-lying states can destroy the phase matching [23,4].

The LIF data in Fig. 5 also show a blueshift in the PFWM excitation curve with respect to the LIF peak. We believe this to be evidence of an ac Stark shift in the $5s$ state due to the presence of a strong 3.4-μm parametric field and as such, no shift is found in the low-density data where the parametric fields are considerably weaker. The shift in the higher-density 1000-ppm signal also indicates that no significant population is transferred when the strong parametric fields are present. This is consistent with suppression of the excited-state population in the two-photon cancellation regime [6,18]. Wunderlich *et al.* [7] have reported that the 330-nm parametric signal can populate the $4s$ level via stimulated Raman scattering which in turn populates the $3p$ level. However, this cannot be a significant effect in these relatively low-sodium-density experiments and accordingly we do not see a recognizable signal in regions where the 330-nm signal is strong.

PFWM was readily observed in sodium nebulized flame such that with sodium densities of between 10^{14} and 10^{15} cm^{-3}, the 330-nm signal was observed to cause significant fluorescence on a white card without the need to focus the pump beam. The 330-nm emission traveled collinearly with the pump beam and was observed by using a UG5 Schott glass filter to block the pump beam while transmitting the 330-nm signal beam. Direct detection of the 330-nm signal with a photomultiplier tube was accomplished by separating the pump and 330-nm signal beams with a Pellin Broca prism. Using this arrangement we investigated the density dependence of the 330-nm signal in the low-density regime. According to Eq. (10), the density dependence of the PFWM signal should be exponential, so for very small signals a near-linear dependence on sodium density can be expected, and this is what we have found. Operation with low sodium concentrations required focusing the beam as shown in the schematic Fig. 4. From the low-concentration data we were able to linearly interpolate the signal-to-noise ratio (SNR) to a sodium density corresponding to SNR$=1$, defining the detection limit. The limit for PFWM detection of sodium in a flame is thus approximately 5×10^{11} atoms/cm^3.

B. Seeded parametric four-wave mixing (SPFWM)

SPFWM was demonstrated using an experimental configuration where the PFWM process in a flame containing a low concentration of sodium was seeded with the infrared PFWM signal generated in a flame containing a high concentration of sodium. We chose to investigate the $3s \rightarrow 4d$ two-photon transition for this study. The $3s \rightarrow 5s$ two-photon transition is not used as the 3.4-μm PFWM signal which is generated could not be efficiently transmitted by any of our available filters. As the PFWM signal generation efficiencies obtained from pumping the $3s \rightarrow 4d$ and $3s \rightarrow 5s$ transitions were comparable, quantitative order-of-magnitude comparisons between our PFWM data and SPFWM data are feasible.

The SPFWM technique relies on the fact that the PFWM process which generates the seeder field and the SPFWM process share the same phase matching conditions so that phase matching of the seeder field is automatically achieved within the SPFWM medium. This property of SPFWM has

already been demonstrated elsewhere in the ability to generate a complex molecular spectrum by simply scanning the pump laser [13]. We have shown in Fig. 5 that a considerable ac Stark shift can be expected in the presence of the strongly focused pump field only when the parametric fields grow sufficiently strong. However, the ac Stark shift must have little effect on the intermediate state, as any significant shift in the intermediate state resonance will quickly compromise the phase matching in the low-density SPFWM medium. It is the presence of the near-resonant 330-nm ultraviolet PFWM signal that balances the effect of the infrared field on the intermediate state and helps preserve the phase matching condition. Fortunately, any shift in the upper state will not alter the phase matching, although it can cause a reduction in the SPFWM gain if the two-photon resonances in the PFWM seeder section and the SPFWM section are significantly separated, effectively producing a self-limiting effect in the maximum gain of the process. This sort of self-limiting can be avoided by using lower pump intensities and greater gain areas in the seeder medium (by modifying the focal conditions), such that the ac Stark shifts are minimized. In this case, by using the $3s \rightarrow 4d$ transition in sodium, which has a strong interaction cross section to the red of the resonance, any small blueshift will be partially compensated by the lineshape asymmetry.

The number density dependence of the SPFWM signal is shown in Fig. 6. This curve shows a strong squared dependence of the signal with Na density as predicted from the simple SPFWM theory in the small signal regime. The higher density data, where the signals are much stronger, departs from the simple small signal behavior. However, in this regime the signal behavior is adequately predicted by the five-level model described by Eqs. (6).

From the small signal number density dependence and by establishing the noise level from the data, the detection limit for SPFWM is determined to be 5×10^9 atoms/cm^3, which is two orders of magnitude better than that found using PFWM alone. We found that operation of our burners at this low concentration was extremely susceptible to sodium contamination. Therefore the detection limit was determined from data using higher concentrations, where contamination errors are less severe. However, we expect that sodium contamination contributed to the noise floor, artificially decreasing our detection sensitivity. In any case, considering all the errors incurred in calculating the sodium concentration within the flame, we expect no more than 50% error in this figure.

In the small signal regime, the SPFWM signal should scale in direct proportion to the seeder field [cf. Eq. (11)]. This is illustrated in the comparison of the excitation scan of the PFWM process with that obtained from the SPFWM process. In the small signal regime we would expect the curves to track each other. This we observe in Fig. 7. The lower curve represents the PFWM signal obtained by nebulizing a 50 000-ppm sodium solution into the flame. If we assume that the infrared field intensity must follow that of the 330-nm signal, which is predicted by the PFWM theory in the limit of no reabsorption, then the SPFWM signal should follow the PFWM curve. For the curve immediately above the PFWM curve, representing the SPFWM signal when nebulizing the flame with a 1.25-ppm Na solution, we find this to be the case, the curve exactly overlaying the PFWM curve within the signal error. This SPFWM signal was quite small and so did not require the use of attenuators and provides a good indication of the level of fluctuation caused by Na contamination in the burner. The top curve represents the SPFWM signal obtained when a 20-ppm signal is nebulized into the burner. In this case the recollimating lens has been adjusted in order to provide a greater gain volume. The subsequent gain increase required significant attenuation of the signal. Here we find that the signal still faithfully tracks the PFWM signal in the wings of the profile; however, the top of the curve departs strongly from the PFWM signal behavior. This represents some type of saturation effect in the strong-signal near-resonance regime. The nature of this effect will be discussed further.

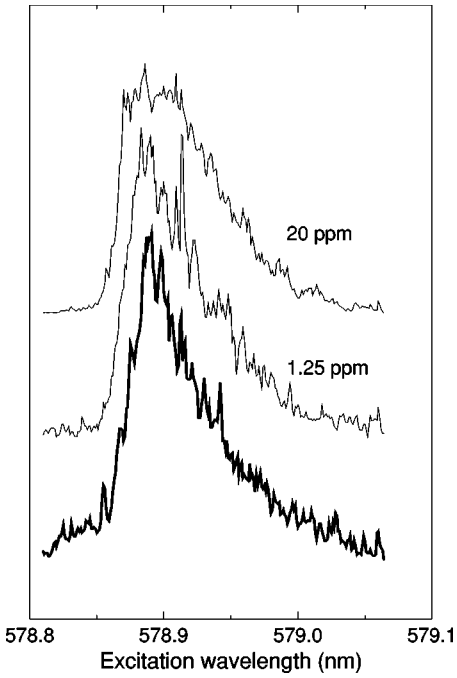

FIG. 7. An excitation scan of both the PFWM (bold curve) and SPFWM (thin curves) signals. The PFWM signal curve is obtained with a 50 000-ppm solution nebulized into the flame. The signal has been strongly attenuated with a cell containing a 1-cm path length of CS_2. The SPFWM excitation scans were obtained using a 50 000 solution in the seeder PFWM section. The two scans represent 1.25-ppm and 20-ppm solutions nebulized into the low-density flame, with the laser providing approximately 7-mJ pulses. The 20-ppm signal was recorded after the recollimating lens was adjusted to increase the SPFWM gain.

C. Saturation behavior

After increasing the gain of the SPFWM process, a saturationlike effect was observed in the SPFWM excitation scan data in Fig. 7. Furthermore, saturationlike behavior is also evident in Fig. 8, where we show the pump power dependence of the SPFWM signal. This pump power dependence shows a total departure from the behavior predicted by the simple perturbation theory treatment of SPFWM [cf. Eqs. (8)]. The curve that is displayed with the power dependence data was generated using the five-level SPFWM model depicted in Fig. 2, which also considers the parasitic FWM process [cf. Eqs. (6)]. The curve is composed of contribu-

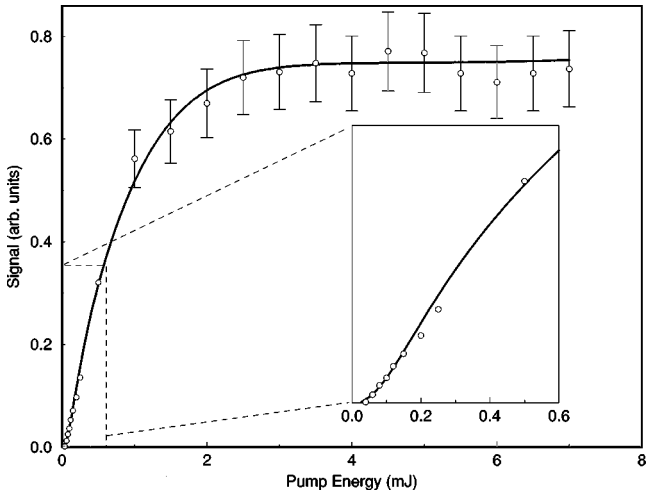

FIG. 8. The SPFWM 330-nm signal dependence on the pump beam energy. The PFWM seeder is nebulized with a 25 000-ppm solution and the low-density flame is nebulized with a 20-ppm sodium solution. The laser is set to a wavelength of 578.88 nm. The data were obtained after the SPFWM gain had been increased by adjusting the recollimating lens. The experimental data (open circles) are displayed along with a simulation curve obtained using the five-level sodium model (solid curve). For clarity, error bars are only shown in the strong signal regime. The inset is used to show the low pulse energy data and simulation curve.

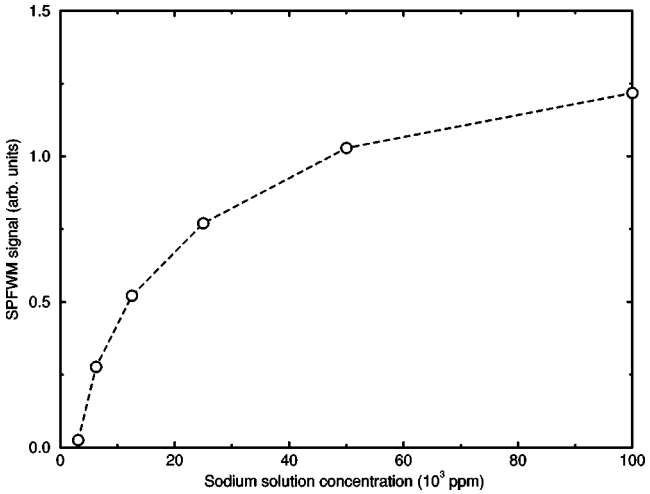

FIG. 9. The SPFWM 330-nm signal dependence on the sodium concentration nebulized into the seeder PFWM flame. The low-density flame is nebulized with a 20-ppm sodium solution with the laser fixed at 578.88 nm and producing approximately 7-mJ pulses. A dashed line joins the data points and is provided simply as a guideline.

tions due to FWM via the $4p_{3/2}$ and $4p_{1/2}$ fine splitting paths with adjustment of the field amplitudes and detunings to provide an adequate fit. The solid curve was generated using the approximation that the amplitudes of the seeded fields remained proportional to the pump field amplitude. This is a reasonable approximation for strong pump fields where the seeder medium is operating near a steady state, but is not suitable for accurately modeling the SPFWM behavior with weak pump fields. Therefore we do not expect the model to perfectly reproduce the small signal behavior depicted in the inset of Fig. 8.

Saturation has been observed in PFWM due to population transfer effects, although the behavior is unlike that of Fig. 8, as an increase in pump power usually increases the rate of population transfer and hence results in a reduction of PFWM signal [22,23,4]. The type of behavior depicted in Fig. 8 would require the increase in SPFWM gain, due to increasing pump power, to exactly balance loss of SPFWM gain, due to increased phase mismatching resulting from pump-induced population transfer. This is highly unlikely. In fact no possible population transfer mechanism is likely to produce the signal behavior observed in Fig. 8. Furthermore, this sort of saturation was not observed for SPFWM in nitric oxide [13].

One of the complicating factors with most atomic species, and sodium in particular, is that there exist many other nearby levels which may give rise to other and competing coherent nonlinear effects. Competition between different FWM processes in sodium has been studied by Chapple *et al.* who show that if the two FWM processes have the appropriate phases, destructive interference results [24]. Spectral analyses of coherent emissions from sodium have shown a number of other fields generated by other effects such as competing FWM processes and stimulated Raman emission [5,7]. In the case of SPFWM, we have used a simple low pass filter which passes the infrared seeder field generated by the PFWM process as well as the infrared fields generated by the parasitic FWM process. So we are in effect seeding both FWM processes. By including both FWM processes in our system model [cf. Eqs. (6)], we are able to predict a signal behavior which is in close agreement with that observed in Fig. 8.

The dependence of the SPFWM signal with varying sodium density in the seeder PFWM process is shown in Fig. 9. This graph indicates that the SPFWM signal increases with increasing sodium concentration in the high-density seeder flame. The last datum of Fig. 8 corresponds to the 25 000-ppm datum in Fig. 9, indicating the saturationlike effect is strongly dependent on the seeding condition. One of the factors governing this behavior is the fact that the 1.18-μm infrared field cannot be collinearly phase matched and so will be emitted at an angle which depends on the sodium density in the seeder medium. Therefore the parasitic FWM process in the low-density medium will be less efficiently coupled as the sodium concentration in the seeder medium increases. Importantly, the signal behavior observed in Fig. 9 is not consistent with population transfer induced saturation, but does support the theory presented in this paper. The operation of SPFWM with relatively low sodium concentrations in the seeder medium provides a good indication of the efficacy of seeder field introduction into the low-density medium.

V. CONCLUSION

We have shown that both PFWM and SPFWM are nondegenerate FWM techniques capable of detecting trace quantities of sodium in a flame environment. Both techniques share the advantage of producing a signal at a wavelength different from that of, but traveling collinearly with, the pump beam, allowing efficient background free signal recovery. PFWM requires the use of tightly focused strong fields

in order to achieve a sufficiently high detection sensitivity. As the PFWM small signal gain is related exponentially to the pump intensity, the gain region is quite well defined, being confined to a volume enclosing the beam waist. Therefore PFWM may be suitable for spatially resolved pointlike measurements. SPFWM, on the other hand, can be operated with lower pump intensities and even unfocused beams and as such may be suitable for remote sensing applications. The increased sensitivity and versatility of SPFWM when compared to PFWM is achieved with little additional complication to the apparatus. Therefore SPFWM should be preferred for sensitive detection applications.

LIF was used to detect intermediate level population that results from the presence of the PFWM fields or the strong pump field. The results indicate that population transfer is not dominant in the PFWM medium. However, an ac Stark shift was observed which was attributed to the presence of strong parametric fields. While the induced ac stark effect shifted the two-photon resonance, it did not adversely affect the phase matching in the SPFWM medium. However, such shifts in the seeder medium two-photon resonance can limit the SPFWM gain. Modification of the focal conditions in the high-density seeder medium should reduce or even remove such shifts and help optimize SPFWM operation.

A theoretical model has been developed which agrees well with the observed SPFWM behavior. The small signal behavior displays simple dependences on both the pump energy and density, suggesting SPFWM may be used for quantitative diagnostic applications. However, the large signal behavior of sodium displayed an anomalous saturationlike effect. This is attributed to competing FWM processes occurring between different intermediate levels in sodium and was adequately modeled by the theory.

We have shown SPFWM to be a sensitive background free optical technique useful for the detection of atomic species. A particular advantage of SPFWM is that it is a simple technique which only requires a single laser and produces a coherent signal which is easily recovered. Its behavior is readily understood in terms of a simple theory which suggests its use as a quantitative diagnostic technique. As SPFWM is a nondegenerate four-wave mixing process, it must satisfy both the appropriate energy balance and phase matching conditions. The extra phase matching constraint restricts SPFWM application to a limited set of atomic and molecular transitions, providing an extra degree of species discrimination. While SPFWM detection of sodium displays a sensitivity which is two orders of magnitude greater than that achieved with PFWM, an increase of four orders of magnitude was reported for SPFWM in nitric oxide [13]. This suggests that optimization of the process should further increase the sensitivity of the technique. The increase in gain afforded by SPFWM may also be useful in increasing the efficiency of FWM based frequency conversion for the generation of VUV radiation.

[1] R. L. Farrow and D. J. Rakestraw, Science **257**, 1894 (1992).
[2] G. Hall and B. Whitaker, J. Chem. Soc. Faraday Trans. **90**, 1 (1994).
[3] G. S. Agarwal, Phys. Rev. Lett. **57**, 827 (1986).
[4] C. R. Vidal, in *Tunable Lasers*, edited by L. F. Mollenauer and J. C. White (Springer-Verlag, Berlin, 1987), pp. 57–113.
[5] W. Hartig, Appl. Phys. **15**, 427 (1978).
[6] M. S. Malcuit, D. J. Gauthier, and R. W. Boyd, Phys. Rev. Lett. **55**, 1086 (1985).
[7] R. K. Wunderlich, W. R. Garrett, R. C. Hart, M. A. Moore, and M. G. Payne, Phys. Rev. A **41**, 6345 (1990).
[8] S. E. Harris, J. E. Field, and A. Imamoğlu, Phys. Rev. Lett. **64**, 1107 (1990).
[9] J. C. Petch, C. H. Keitel, P. L. Knight, and J. P. Marangos, Phys. Rev. A **53**, 543 (1996).
[10] U. Czarnetzki and H. F. Döbele, Phys. Rev. A **44**, 7530 (1991).
[11] G. Z. Zhang, K. Hakuta, and B. P. Stoicheff, Phys. Rev. Lett. **71**, 3099 (1993).
[12] M. Jain, G. Y. Yin, J. E. Field, and S. E. Harris, Opt. Lett. **18**, 998 (1993).
[13] M. J. Fernée, P. F. Barker, A. E. W. Knight, and H. Rubinsztein-Dunlop, Phys. Rev. Lett. **79**, 2046 (1997).
[14] M. J. Fernée, P. F. Barker, H. Rubinsztein-Dunlop, and A. E. W. Knight, J. Chem. Phys. (to be published).
[15] D. J. Harter, P. Narum, M. G. Raymer, and R. W. Boyd, Phys. Rev. Lett. **46**, 1192 (1981).
[16] R. W. Boyd, M. G. Raymer, P. Narum, and D. J. Harter, Phys. Rev. A **24**, 411 (1981).
[17] R. Loudon, *The Quantum Theory of Light*, 2nd ed. (Clarendon, Oxford, 1983).
[18] R. W. Boyd, M. S. Malcuit, D. J. Gauthier, and K. Rzażewski, Phys. Rev. A **35**, 1648 (1987).
[19] W. L. Wiese, M. W. Smith, and B. M. Miles, *Atomic Transition Probabilities, Sodium to Calcium*, Natl. Bur. Stand. Ref. Data Ser., Natl. Bur. Stand. (U.S.) Circ. No. NSRDS-NBS22 (U.S. GPO, Washington, DC, 1969), Vol. II.
[20] P. F. Barker and H. Rubinsztein-Dunlop, Spectrochim. Acta B **50**, 1301 (1995).
[21] M. A. Moore, W. R. Garrett, and M. G. Payne, Opt. Commun. **64**, 310 (1988).
[22] H. Scheingraber and C. Vidal, IEEE J. Quantum Electron. **QE-19**, 1747 (1983).
[23] J. Heinrich, K. Hollenberg, and W. Behmenburg, Appl. Phys. B: Photophys. Laser Chem. **33**, 225 (1984).
[24] P. B. Chapple, K. G. Baldwin, and H. A. Bachor, J. Opt. Soc. Am. B **6**, 180 (1989).